Angular distribution measurement for ^{12}C fragmentation via ^{12}C + ^{12}C scattering at 100 MeV/u[*]

Wei-Wei Qu(屈卫卫)[1,2]   Gao-Long Zhang(张高龙)[3,4;1)]   Guo-Yu Tian(田国玉)[5]

Zhi-Qiang Chen(陈志强)[5]   Shou-Ping Xu(徐寿平)[6]   Royichi Wada[7]

[1] State Key Laboratory of Radiation Medicine and Protection, School of Radiation Medicine and Protection, Soochow University, Suzhou 215123, China
[2] Collaborative Innovation Center of Radiological Medicine of Jiangsu Higher Education Institutions, Suzhou 215123, China
[3] School of Physics and Nuclear Energy Engineering, Beihang University, Beijing 100191, China
[4] Beijing Advanced Innovation Center for Big Data-based Precision Medicine, Beihang University, Beijing, 100083, China
[5] Institute of Modern Physics, Chinese Academy of Sciences, Lanzhou 730000, China
[6] Department of Radiation Oncology, PLA General Hospital, Beijing 100853, China
[7] Cyclotron Institute, Texas A& M University, College Station, Texas 77843, USA

Abstract: The angular distributions and energy spectra of ^{11}B, ^{10}B, and ^{9}Be fragments of ^{12}C in the angular range from 1.0° to 7.5° at 100 MeV/u were obtained via ^{12}C + ^{12}C scattering. Detailed comparisons are presented between the experimental data and the modified antisymmetrized molecular dynamics (AMD-FM), binary intranuclear cascade model (BIC) and Liège intranuclear cascade model (INCL++). The experimental angular distributions and energy spectra are well reproduced by the AMD-FM calculations but fail to be reproduced by the physical models installed in the Geant4 program, including the BIC and INCL++ models.

Keywords: breakup, angular distribution, AMD, Geant4 simulation

PACS: 25.60.Gc, 13.85.Dz, 13.85.Fb   **DOI:** 10.1088/1674-1137/42/7/074001

1   Introduction

Studies of the mechanisms of ion fragmentation in collisions with incident energies of 10–1000 A MeV have drawn much attention due to the possible applications in space [1, 2] and particle therapy [3]. Simulation codes are often used in such applications, and their accuracy relies on the physical processes implemented. The models used in these applications are often insufficient to reproduce the fragmentation processes with the required accuracy and need to be validated using experimental data. However, fragmentation cross sections of light ions on thin targets are scarce. The incident energy should be covered up to 400 MeV/u according to the possible beam energies in particle therapy and space detection. Moreover, the energy density of intermediate mass fragments (IMFs) passing through a substance is much higher than that of light charged particles, and therefore the proper amount of IMF production is crucial for the simulation. In order to achieve the proper production rate, it is essential to understand the production mechanism of these IMFs. Their total cross section is dominated by the projectile-like fragment component ($\theta_{\mathrm{lab}} \leqslant 10°$). Therefore, in this paper we focus on the production of IMFs at very forward angles.

To improve the models in Monte Carlo simulations, several experiments on thin targets have been performed. An experiment was performed using 62 MeV/u ^{12}C on a carbon target in Catania, Italy [4]. The results showed that discrepancies are up to one order of magnitude for both angular and energy distributions in comparison with the GEANT4 simulation. Another experiment was performed using 400 MeV/u ^{12}C on a carbon target at the Gesellschaft fur SchwerIonenforschung (GSI, Germany) by the FIRST collaboration [5]. This experiment presented the single differential cross sections of carbon-ion fragmentation on a thin gold target, measured as a function of the fragment angle and kinetic energy in the forward angular region of $\theta \leqslant 6°$, aiming to provide useful data for the benchmarking of the simulation software used in light ions fragmentation applications. This experimental input is highly valuable, as it sets a reference point. A third experiment was performed at GANIL in 2011 to study ^{12}C reactions on C, H, O, Al, and Ti tar-

gets at 95 MeV/u [6]. The angular range covered from 4° to 43°. To complete these data, another experiment was performed in 2013 [7] at GANIL to measure the fragmentation cross section at 0° for 95 MeV/u ^{12}C beam on thin targets. Angular distributions and energy spectra of projectiles were compared with the reaction models embedded in the GEANT4 Monte Carlo toolkit [6, 8]. In that comparison, none of the models provide good enough reproduction of the experimental data, especially for those from intermediate velocity sources [9]. Previous comparisons also showed that the angular distributions were better reproduced by the binary intranuclear cascade (BIC) model than the quantum molecular dynamics (QMD) model. Detailed comparisons between the experimental data of ^{12}C + ^{12}C at 95 MeV/u and transport model simulations were presented for all charged particles and fragments. The experimental energy spectra and angular distributions are well reproduced by the AMD-FM calculations for light charged particles with $Z \leqslant 2$ [9]. The angular distributions of isotopes with $Z \geqslant 2$ were qualitatively reproduced reasonably well, but the yields are 2-10 times smaller in the simulations for most isotopes.

The elastic and inelastic scatterings of ^{12}C + ^{12}C with an incident energy of 100 MeV/u [10–12] and 200 MeV/u [13] have been published to study the repulsive three-body force in high density nuclear matter. Fragments such as ^{11}B, ^{10}B, and ^{9}Be were produced together with the elastic and inelastic scatterings of ^{12}C. Therefore, the differential cross sections for these fragments has been extracted. This work aims to provide reference data for ^{12}C fragmentations at 100 MeV/u and further explore the reaction mechanism of the fragmentation process.

This paper is organized as follows. Section 2 describes the experimental procedure. The experimental differential cross section is presented in Section 3. Section 4 presents the theoretical methods. Comparisons between the theoretical results and the experimental data are shown in Section 5. A summary is given in Section 6.

2   Experimental procedure

Scattering for ^{12}C + ^{12}C was measured at an incident energy of 100 MeV/u (1.2 GeV) at the Ring Cyclotron Facility of the Research Center of Nuclear Physics (RCNP) in Osaka University. The high-resolution spectrometer Grand Raiden was used for the measurements. Details of the experimental setup can be found in Ref. [11].

A Monte Carlo simulation was performed to obtain a small beam size and better angular resolution on target [14]. A solution without collimation could be used based on the simulation. Angular spread of 0.05° (1σ)

or smaller was obtained in an achromatic focusing condition. The beam size was less than 2 mm (radius) on the target. The angular resolution of 0.105° (FWHM) in the present experiment was confirmed by faint ^{12}C primary beam with an empty target run. In this measurement, the scattering angle in the laboratory frame covered from 1.0° to 7.5°. The acceptances of the spectrometer in the horizontal and vertical directions were set to ± 20 mrad and ± 6 mrad by the collimators placed at the entrance of the spectrometer, respectively. The momentum acceptance is about 5%. To guarantee a slight overlap of the scattering angles between the different angular settings, the central scattering angles of the Grand Raiden spectrometer were set to 2.0°, 2.5°, 3.5°, 5.0° and 6.5°. The two obtained cross sections at different angular settings of the magnetic spectrometer were not completely consistent with each other. These differences were less than 25% and treated as systematic errors.

In this experiment the beam intensity varied from 0.1 to 1.0 pnA on the target. A natural carbon target with a thickness of 1.18 mg/cm^2 and a polyethylene film with a thickness of 11.40 mg/cm^2 were used for the measurements. Details of the detector system can also be found in Ref. [11].

Particles were identified by the energy loss (ΔE) - time of flight (TOF) information obtained from the plastic scintillation detectors on the focal plane. The accelerator radio frequency signal was used as the start signal in the TOF measurement. The particle identification results are shown in Fig. 1. Six isotopes were clearly separated. The central momenta for each isotope were obtained by the magnet rigidity of each run setting. The obtained velocities for each isotopes were consistent with the calculated results, depending on the mean orbit radius, total deflection angle of the magnet spectrometer, and the radio frequency of the accelerator.
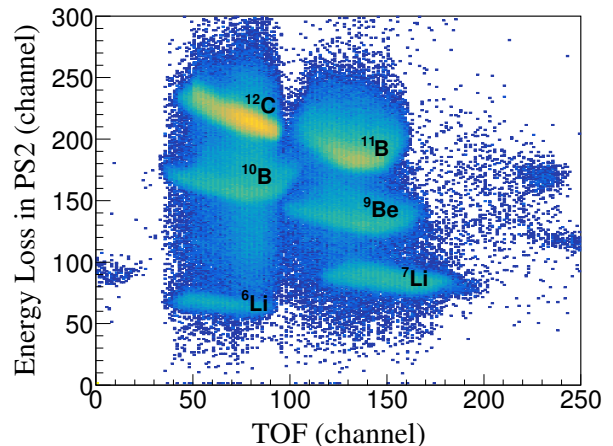

Fig. 1.   (color online) Particle identification in ^{12}C + ^{12}C scattering experiment.

Due to the limited vertical acceptance compared to the horizontal acceptance, the spread of the vertical angles was not taken into account. Therefore, the horizontal scattering angles were obtained from the beam optical matrix of the spectrometer and information from the focal plane detectors.

3   Differential cross section

The differential cross section for specific fragments is calculated by

$$\frac{\mathrm{d}\sigma}{\mathrm{d}\Omega} = \frac{N/\varepsilon_{\mathrm{d}}\varepsilon_{\mathrm{t}}\varepsilon_{\mathrm{a}}}{N_0 N_{\mathrm{T}} \Omega}, \tag{1}$$

where N is the number of detected fragments, ε_{d} is the detection efficiency for fragments, ε_{t} is the data acquisition system trigger efficiency, ε_{a} is the efficiency for data analysis, N_0 is the number of incident nuclei, N_{T} is the number of target nuclei per square centimeter, and Ω is the solid angle for present detection.

A Faraday cup connected to a current integrator was used to collect the total charge of the incident particles. In the calculation of the differential cross section, the efficiencies, including ε_{d}, ε_{t} and ε_{a}, could be determined from the data itself [11, 15]. The differential cross sections for the observed fragments in the present experiment are extracted based on Eq. (1). Here, the uncertainties of the beam intensity, target thickness, solid angle and efficiencies were taken into account. Systematic errors of $\pm 25\%$ were added for the absolute values of the cross sections according to the different angular settings of the spectrometer.

4   Theoretical models

4.1   AMD model

In the AMD model, the wave function of a N-nucleon system is described by a Slater determinate of N Gaussian wave packets [16]

$$\Phi(Z) = \det \left\{ \exp \left[-\nu \left(\boldsymbol{r}_j - \frac{\boldsymbol{Z}_i}{\sqrt{\nu}} \right)^2 + \frac{1}{2} \boldsymbol{Z}_i^2 \right] \chi_{\alpha_i}(j) \right\}, \tag{2}$$

where the complex variables $Z \equiv \{\boldsymbol{Z}_i; i = 1,...,N\} = \{Z_{i\sigma}; i = 1,...,N, \sigma = x,y,z\}$ denote the centroids of the wave packets. The label α_i denotes the spin and isospin of the i-th single particle state of $p\uparrow$, $p\downarrow$, $n\uparrow$, or $n\downarrow$. ν is the width parameter, taken as $\nu = 0.16$ fm^{-2}, which is optimized to reproduce the experimental binding energy of nuclei. The time evolution of $\boldsymbol{Z}_i$ is determined by the time-dependent variational principle and the two-body nucleon collision process. The equation of motion for Z is derived as

$$i\hbar \sum_{j\tau} C_{i\sigma,j\tau} \frac{\mathrm{d}Z_{j\tau}}{\mathrm{d}t} = \frac{\partial \mathcal{H}}{\partial Z_{i\sigma}^*}, \tag{3}$$

where $\mathcal{H}$ represents the Hamiltonian and $C_{i\sigma,j\tau}$ represents a Hermitian matrix which is defined as

$$C_{i\sigma,j\tau} = \frac{\partial^2}{\partial Z_{i\sigma}^* \partial Z_{j\tau}} \log \langle \Phi(Z) | \Phi(Z) \rangle. \tag{4}$$

In the AMD model, the centroid of the wave packet in the ground state nucleus momentum space in the initial nuclei is set to nearly zero. It means the initial nuclei are "frozen", so that makes the initial nuclei stable in time. The AMD model deals with the nucleon-nucleon collision process in physical coordinate space. Here, the physical coordinate $W \equiv \{\boldsymbol{W}_i\}$ for a given nucleon i is defined as

$$\boldsymbol{W}_i = \sum_{j=1} A(\sqrt{Q})_{ij} \boldsymbol{Z}_j, \tag{5}$$

where the Q_{ij} is defined as

$$Q_{ij} = \frac{\partial}{\partial (Z_i^* Z_j)} \ln \langle \Phi(\boldsymbol{Z}) | \Phi(\boldsymbol{Z}) \rangle. \tag{6}$$

The Winger form of the i-th nucleon at time $t = t_0$ is described by

$$f_i(\boldsymbol{r},\boldsymbol{p},t_0) = 8\exp \left\{ -2\nu(\boldsymbol{r} - \boldsymbol{R}_i(t_0))^2 - \frac{(\boldsymbol{p} - \boldsymbol{P}_i(t_0))^2}{2\hbar^2 \nu} \right\}, \tag{7}$$

with centroid $\boldsymbol{R}_i$ and $\boldsymbol{P}_i$. The sum of f_i is the total one-body distribution function. It is valid approximately only when the physical coordinate

$$\boldsymbol{W}_i = \sqrt{\nu} \boldsymbol{R}_i + \frac{i}{2\hbar\sqrt{\nu}} \boldsymbol{P}_i \tag{8}$$

is used for the centroid of the Gaussian wave packets [16]. Similar to other transport models, two important processes exist in AMD model. The first is the mean field propagation of nucleons and the other is the nucleon-nucleon (NN) collision process. The Pauli principle is fully respected in an exact manner in both processes in the AMD model. The Gogny interaction [17] is used for the mean field in the present work. The nucleon-nucleon cross section is described by [18]

$$\sigma(E,\rho) = \min \left(\sigma_{\mathrm{LM}}(E,\rho), \ \frac{100 \ \mathrm{mb}}{1 + E/200 \ \mathrm{MeV}} \right), \tag{9}$$

where $\sigma_{\mathrm{LM}}(E,\rho)$ represents the cross section given by Li and Machleidt [19, 20].

4.2   AMD-FM model

The AMD-FM model was originally developed for the description of the high energy proton spectra in intermediate heavy-ion collisions [21]. In AMD-FM, the Fermi motion is considered in the two body collision process. If two nucleons reach the collision distance $\sqrt{\sigma_{\mathrm{NN}}/\pi}$, the uncertainty of momentum will increase. This momentum uncertainty is obtained along the Gaussian distribution

around the centroid of the Gaussian wave packets. Compared to other transport models, in which the Fermi motion is only given once in initial nuclei, this treatment is more proper.

In practical calculations for given coordinate vectors $\boldsymbol{r}_1$ and $\boldsymbol{r}_2$ of two collision nucleons, the corresponding momenta $\boldsymbol{P}_1$ and $\boldsymbol{P}_2$ are given by

$$\boldsymbol{P}_i = \boldsymbol{P}_i^0 + \Delta \boldsymbol{P}_i' \qquad (i=1,2), \qquad (10)$$

where $\boldsymbol{P}_i^0$ represents the centroid of the Gaussian momentum distribution for the i-th particle and $\Delta \boldsymbol{P}_i'$ represents the Fermi momentum given randomly along the Gaussian distribution. Due to the momentum distribution being partially considered in the wave packet propagation, T_0, which represents an average value of the Gaussian momentum distribution, is subtracted from $\Delta \boldsymbol{P}_i'$ to avoid double counting. $T_0 = 9.20$ MeV is used for the Gogny interaction. After the subtraction of T_0, $\Delta \boldsymbol{P}_i'$ is obtained by

$$\Delta \boldsymbol{P}_i' = \sqrt{\left(\frac{|\Delta \boldsymbol{P}_i|^2}{2M_0} - T_0\right)2M_0}\frac{\Delta \boldsymbol{P}_i}{|\Delta \boldsymbol{P}_i|}, \qquad (11)$$

$$\Delta P_{i\tau} = \hbar\sqrt{\nu}(\rho_i/\rho_0)^{1/3}G(1), \qquad (12)$$

where $G(1)$ represents a random number generated throughout the Gaussian distribution with $\sigma = 1$. The parameter $(\rho_i/\rho_0)^{1/3}$ in Eq. (16) is used for considering the density dependence of the Fermi energy, and ρ_i and ρ_0 are the density at $\boldsymbol{r}_i$ and the normal nuclear density, respectively. τ denotes the x,y,z coordinates. $\Delta \boldsymbol{P}_i'$ is set to zero when $|\Delta \boldsymbol{P}_i|^2/2M_0 < T_0$.

If the collision is Pauli-blocked, the treatment in the W space is revocatory and the time evolution of wave packets continues in the Z space. Inversely, if the collision is Pauli-allowed, the energy and momentum conservation are restored. The energy restoration is obtained within the cluster by

$$\Delta E = \left(\sum_{i,\sigma}\frac{\partial \mathcal{H}}{\partial Z_{i,\sigma}} \cdot \frac{\mathrm{d}Z_{i,\sigma}}{\mathrm{d}t}\right)\Delta t, \qquad (13)$$

where $\mathcal{H}$ represents the Hamiltonian of the cluster and Δt is used as an artificial fine step for turning.

4.3 Geant4 simulations

Based on the Monte Carlo method, the Geant4 program can provide various particle generators which can be used to simulate the propagation of particles through various nuclear matter by interpolating different physical models [22]. Nuclear reactions at intermediate energies (varies from few MeV to several GeV) are typically described in two stages. The first, which is the fast reaction stage, can be described by a dynamical model (such as quantum molecular dynamics, pre-compound, intranuclear cascade and so on), and results in the production of particles with one or several excited nuclei [23]. The second reaction stage describes the de-excitation of the produced excited nuclei in the first stage and it is usually described by statistical de-excitation models.

For the first stage of the collision, there are several nuclear reaction models which are recommended in the Geant4 toolkit for hadron therapies. The first is a binary intranuclear cascade (BIC) model [23]. The BIC in Geant4 deals with an intranuclear cascade propagating primary and secondary particles in a nucleus. Interactions between a primary or secondary particle and an individual nucleon of the target nucleus are taken into account. Particle propagation in the nuclear field is performed by numerically solving the equation of motion. The cascade stops when the average and maximum energies of secondaries are smaller than a given threshold. For the remaining fragment, it is treated by the precompound and de-excitation models.

The second model is the Liège intranuclear cascade model (INCL++) [8, 23–25]. INCL++ is a model which incorporates cascade physics principles [23]. It is used to simulate the collision process between incident particles and nuclei. The positions and momenta of the nucleons inside the nuclei are determined from the beginning of the simulation by treating the nucleus as a free Fermi gas in a static potential with realistic density. The cascade is modeled by tracking those nucleons and their collisions.

For the second stage of the nuclear reaction in the present work, the ABLA V3 model was used. The ABLA V3 evaporation model uses excited nucleus parameters including excitation energy, mass number, charge number and nucleus spin as input quantities [23]. The probabilities for emitted protons, neutrons, alpha particles and clusters can be calculated. The couplings of the ABLA V3 to the BIC and INCL++ models were used according to the manual [26].

5 Results and discussion

The experimental energy spectra were normalized by the method of Ref. [6]

$$\frac{\mathrm{d}\sigma}{\mathrm{d}\Omega}(^A_Z X) = \frac{N_{^A_Z X} \times A_{\text{target}}}{N_{^{12}\text{C}} \times \Omega \times \rho \times th \times N_{\text{A}}}, \qquad (14)$$

where $N_{^A_Z X}$ is the number of $^A_Z X$ fragments detected, A and Z are the mass and charge of fragment X, respectively, A_{target} is the target mass, $N_{^{12}\text{C}}$ is the number of incident carbon nuclei, Ω is the solid angle of the detector, $\rho \times th$ is the target area density and N_{A} is Avogadro's number.

The energy spectra and angular distributions of the obtained differential cross sections of ^{12}C fragmentation on a natural carbon target are indicated in Fig. 2 and Fig. 3 by solid circles, respectively. In Fig. 2, the peak

positions of all fragments correspond to the projectile-like fragmentation. Sharp fall-offs of energy distributions for all fragments on both sides of the energy peak are observed, since the magnetic rigidity and acceptance of magnetic spectrometer are set according to the scattered ^{12}C kinematics. This phenomenon is similar to those of Refs. [5–7]. In Fig. 3, the differential cross sections decrease with the increase of scattering angles. With the decrease of scattering angles, the cross sections of ^{11}B fragments increase faster than those of ^{9}Be and ^{10}B, especially at very small angles. This is similar to the results of Refs. [5–7]. The trends of our present data are consistent with those of the published data [5–7] within the angular and differential cross section error bars. However, the published data focused on a large angular range, and the angular resolution was large ($\sim 10°$). In our work the angular resolution is better ($\sim 0.1°$) at small angles ($\theta_{\text{lab}} \leq 10°$), which is very important for understanding the production mechanism of these IMFs.

The energy spectra for ^{11}B, ^{10}B, and ^{9}Be fragments were obtained by the AMD-FM model and Geant4 with two physical models and the results are shown in Fig. 2. The solid lines represent the results of the AMD-FM model. The dashed lines and dot-dashed lines represent the results obtained by the INCL++ and BIC models, respectively. The obtained energy spectrum was normalized for each model. The filled dots denote the experimental data. The sharp fall-offs of the experimental energy spectra are partially due to the magnetic rigidity and acceptance of the magnetic spectrometer which was introduced in Section **2**. As shown in Fig. 2, the energy spectra for all fragments can be reproduced reasonably well by the AMD-FM model. However, the same trend by the BIC model was not obtained. The BIC model shows a sharp peak structure and obvious shifts from those of the experiments. The INCL++ model reproduced the experimental values well for the ^{11}B fragments, but not so well for the ^{9}Be and ^{10}B fragments. Depending on the reaction mechanism, there are three components during the nuclear collision, including projectile-like fragments (PLF), target-like fragments (TLF), and nucleon-nucleon fragments (NN). In the theoretical models, all three components (PLF, TLF and NN) are taken into account in both AMD and INCL++ models. However, only the PLF component is taken into account in the BIC model, which treats this intermediate mass reaction as a two-body collision process without NN and TLF components. The BIC model also shows poor reproduction of experimental data in Ref. [8] due to the binary nature of the reaction mechanism assumed in the model. This is the reason why there is a sharp cut in Fig. 2 for the BIC model. The INCL++ model gives better energy spectra reproduction than those of BIC model. It indicates that the INCL++ model can describe the reaction
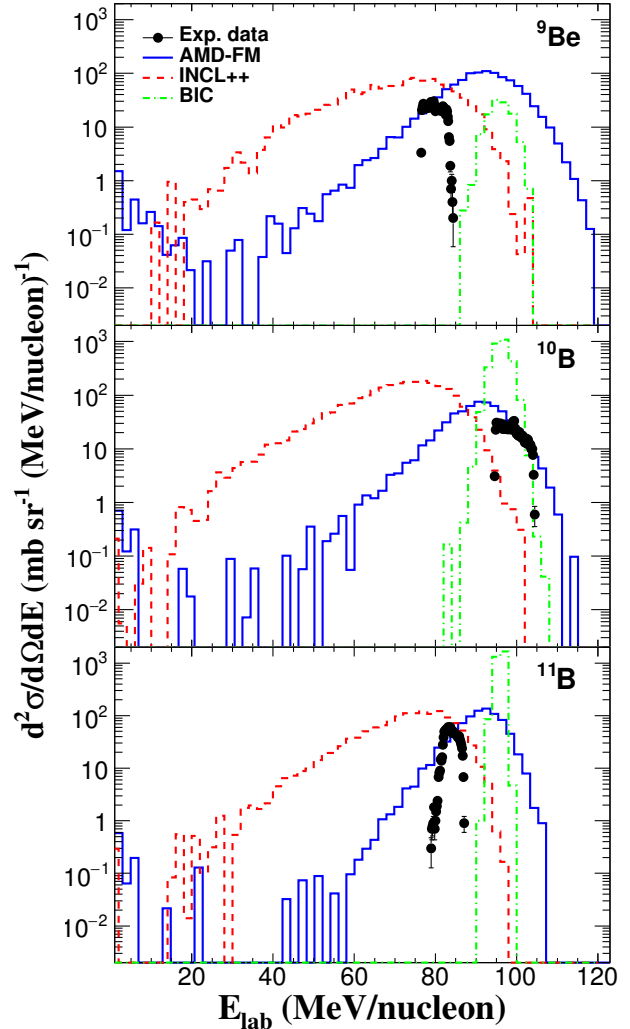
process reasonably, more or less as the AMD model.

Fig. 2.   (color online) The energy spectra for ^{11}B, ^{10}B, and ^{9}Be fragments via ^{12}C + ^{12}C scattering, with angular range from 3.0° to 4.0°, in the laboratory frame. The solid lines present the results obtained using the AMD-FM model. The filled circles denote the experimental data. Here, the magnet rigidity value was 2.95 Tm.

The angular distributions of differential cross sections for ^{11}B, ^{10}B, and ^{9}Be fragments are shown in Fig. 3. Due to the magnetic rigidity and acceptance of the magnetic spectrometer, the particle momentum out of the acceptance cannot reach the focal plane detectors. Therefore, the energy thresholds have been taken into account in the INCL++ and AMD-FM calculations. As an obvious shift peak position between the experimental data and BIC simulation was obtained, a momentum acceptance of 5% was used to renormalize the simulation results. The solid lines present the calculated angular distribu-

tion of differential cross section by the AMD-FM model, and the dashed and dot-dashed lines represent the simulated results of the INCL++ and BIC models, respectively.
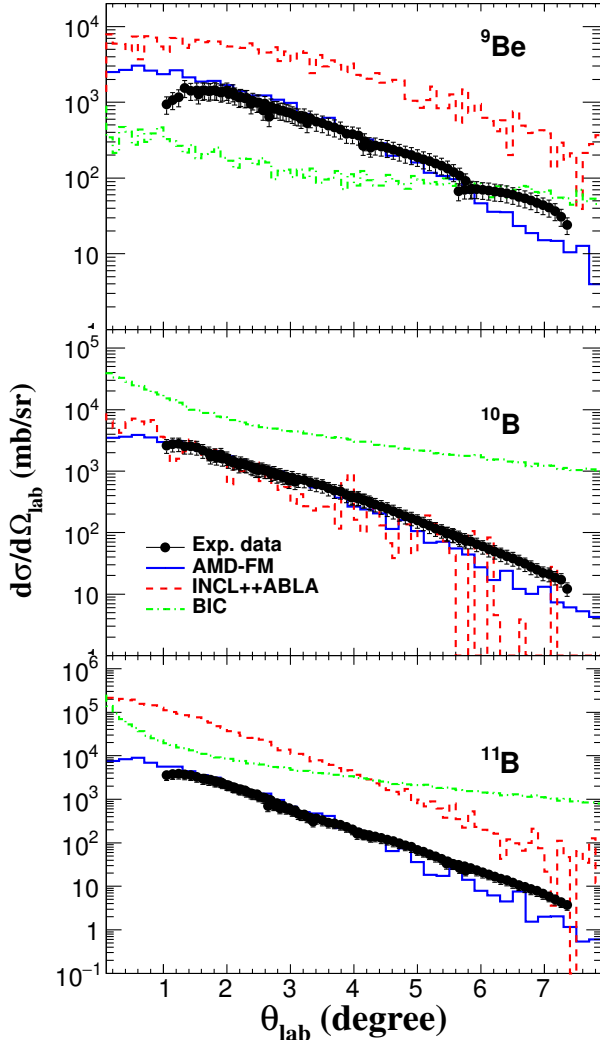

Fig. 3.   (color online) The angular distributions of differential cross sections for ^{11}B, ^{10}B, and ^{9}Be fragments via ^{12}C + ^{12}C scattering. The solid lines present the differential cross section angular distribution obtained using the AMD-FM model. The filled circles denote the experimental data.

As shown in Fig. 3, the calculated differential cross sections for ^{9}Be by the AMD-FM model reproduce the experimental data reasonable well from 1.5° to 4.0°. For large angles, the experimental results are higher than the calculation. The calculated angular distribution by the BIC model in the Geant4 toolkit reproduced the data reasonably well from 5.5° to 7.0°. However, the BIC

model underestimates the absolute differential cross sections by an order of magnitude at small angles. The INCL++ model overestimates the differential cross sections by a factor of 2 or 3 at small angles and 5 at large angles.

For the ^{10}B case, the experimental data are smoother. Both the AMD-FM and INCL++ models can reproduce the experimental data reasonably well at small angles. At angles larger than 5°, the calculated differential cross section underpredicts the experimental value slightly, by a factor of up to 2. However, the BIC model overestimates the differential cross sections by a factor of nearly 10 at small angles and more than 100 at large angles, compared with the experimental data.

For the ^{11}B fragments, the AMD-FM model underestimates the experimental data when the angle is larger than 4.0°, which is very similar to the ^{10}B case. The BIC still overpredicts the experimental data, as for the ^{10}B case but with less difference. The INCL++ model overestimates the differential cross sections through the whole angular range by an order of magnitude.

The experimentally measured isotopes' energy spectra and differential cross section angular distributions in ^{12}C + ^{12}C collisions can be reproduced by the AMD-FM model reasonably well, but not by Geant4 simulations with the INCL++ and BIC models.

6   Summary

The angular distributions and energy spectra of ^{9}Be, ^{10}B, and ^{11}B isotopes from ^{12}C fragmentation via ^{12}C + ^{12}C scattering at 100 MeV/nucleon in the angular range of 1.0°-7.5° have been measured and compared with theoretical calculations. The present experimental data are consistent with respect to the previous data. Detailed comparisons were made between the experimental data and the modified antisymmetrized molecular dynamics (AMD-FM) and Geant4 with BIC and INCL++ models. For the three isotopes measured experimentally, ^{9}Be, ^{10}B and ^{11}B, the angular distributions can be reproduced reasonably well with the AMD-FM model. However, the physical models used in the Geant4 program cannot reproduce the experimental data well for all those isotopes simultaneously. The present data provide valuable reference data for the physical models used in Monte Carlo simulations. To further improve the simulation accuracy and apply the models in therapy, space applications etc, further experimental data are needed.

References

1 M. Durante and F. A. Cucinotta, Rev. Mod. Phys., **83**: 1245 (2011)
2 Z. W. Lin, Phys. Rev. C, **75**: 034609 (2007)
3 D. Schardt, T. Elsasser, and D. Schulz-Ertner, Rev. Mod. Phys., **82**: 383 (2010)
4 M. De Napoli et al, Phys. Med. Biol., **57**: 7651 (2012)
5 M. Toppi et al, Phys. Rev. C, **93**: 064601 (2016)
6 J. Dudouet, D. Juliani, M. Labalme, D. Cussol, J. C. Angélique, B. Braunn, J. Colin, Ch. Finck, J. M. Fontbonne, H. Guérin, P. Henriquet, J. Krimmer, M. Rousseau, M. G. Saint-Laurent, and S. Salvador, Phys. Rev. C, **88**: 024606 (2013)
7 J. Dudouet, M. Labalme, D. Cussol C. Finck, R. Rescigno, M. Rousseau, S. Salvador, and M. Vanstalle, Phys. Rev. C, **89**: 064615 (2014)
8 J. Dudouet, D. Cussol, D. Durand, and M. Labalme, Phys. Rev. C, **89**: 054616 (2014)
9 G. Tian, R. Wada, Z. Chen, R. Han, W. Lin, X. Liu, P. Ren, F. Shi, F. Luo, Q. Sun, L. Soog, and G. Q. Xiao, Phys. Rev. C, **95**: 044613 (2017)
10 W. W. Qu, G. L. Zhang, S. Terashima, T. Furumoto, Y. Ayyad, Z. Q. Chen, C. L. Guo, A. Inoue, X. Y. Le, H. J. Ong, D. Y. Pang, H. Sakaguchi, Y. Sakuragi, B. H. Sun, A. Tamii, I. Tanihata, T. F. Wang, R. Wada, and Y. Yamamoto, Phys. Lett. B, **751**: 1 (2015)
11 W. W. Qu, G. L. Zhang, S. Terashima, T. Furumoto, Y. Ayyad, Z. Q. Chen, C. L. Guo, A. Inoue, X. Y. Le, H. J. Ong, D. Y. Pang, H. Sakaguchi, Y. Sakuragi, B. H. Sun, A. Tamii, I. Tani-hata, T. F. Wang, R. Wada, and Y. Yamamoto, Phys. Rev. C, **95**: 044616 (2017)
12 W. W. Qu, G. L. Zhang, S. Terashima, Isao Tanihata, C. L. Guo, and X. Y. Le, Nucl. Sci. and Tech., **25**: 050501 (2014)
13 W. W. Qu, G. L. Zhang, S. Terashima, C. L. Guo, I. Tanihata, X. Y. Le, T. F. Wang, X. H. Zhang, Z. Y. Sun, L. M. Duan, R. J. Hu, C. G. Lu, P. Ma, Nucl. Instrum. Methods Phys. Res. Sect. A, **832**: 243 (2016)
14 W. W. Qu, G. L. Zhang, I. Tanihata, S. Terashima, C. L. Guo, X. Y. Le, and H. Sakaguchi, Chin. Phys. C, **38**: 116202 (2014)
15 W. W. Qu, Study of three-body force via ^{12}C + ^{12}C scattering at 100A MeV:[D], (Beijing: Beihang University, 2015)
16 A. Ono, H. Horiuchi, Toshiki Maruyama, and A. Ohnishi, Prog. Theor. Phys., **87**: 1185 (1992)
17 J. Dechargé and D. Gogny, Phys. Rev. C, **21**: 1568 (1980)
18 A. Ono, Phys. Rev. C, **59**: 853 (1999)
19 G. Q. Li and R. Machleidt, Phys. Rev. C, **48**: 1702 (1993)
20 G. Q. Li and R. Machleidt, Phys. Rev. C, **49**: 566 (1994)
21 W. Lin, X. Liu, R. Wada, M. Huang, P. Ren, G. Tian, F. Luo, Q. Sun, Z. Chen, G. Q. Xiao, R. Han, F. Shi, J. Liu, and B. Gou, Phys. Rev. C, **94**: 064609 (2016)
22 S. Agostinelli et al, Nucl. Instrum. Methods Phys. Res. Sect. A, **506**: 250-303 (2003)
23 Geant4 Physics ReferenceManual (Version 10.0), (2013)
24 D. Mancusi, A. Boudard, J. Cugnon, Jean-Christophe David, P. Kaitaniemi, and S. Leray, Phys. Rev. C, **90**: 054602 (2014)
25 A. Boudard, J. Cugnon, J. C. David, S. Leray, and D. Mancusi, Phys. Rev. C, **87**: 014606 (2013)
26 Geant4 User's Guide for Application Developers (Version: geant4 10.3): (2016)